

Electrotunable Nanoplasmonics for Amplified Surface Enhanced Raman Spectroscopy

Ye Ma, Debabrata Sikdar, Aleksandra Fedosyuk, Leonora Velleman, Daniel J Klemme, Sang-Hyun Oh, Anthony R. J. Kucernak, Alexei A. Kornyshev, and Joshua B. Edel

ACS Nano, **Just Accepted Manuscript** • DOI: 10.1021/acsnano.9b05257 • Publication Date (Web): 06 Dec 2019

Downloaded from pubs.acs.org on December 6, 2019

Just Accepted

“Just Accepted” manuscripts have been peer-reviewed and accepted for publication. They are posted online prior to technical editing, formatting for publication and author proofing. The American Chemical Society provides “Just Accepted” as a service to the research community to expedite the dissemination of scientific material as soon as possible after acceptance. “Just Accepted” manuscripts appear in full in PDF format accompanied by an HTML abstract. “Just Accepted” manuscripts have been fully peer reviewed, but should not be considered the official version of record. They are citable by the Digital Object Identifier (DOI®). “Just Accepted” is an optional service offered to authors. Therefore, the “Just Accepted” Web site may not include all articles that will be published in the journal. After a manuscript is technically edited and formatted, it will be removed from the “Just Accepted” Web site and published as an ASAP article. Note that technical editing may introduce minor changes to the manuscript text and/or graphics which could affect content, and all legal disclaimers and ethical guidelines that apply to the journal pertain. ACS cannot be held responsible for errors or consequences arising from the use of information contained in these “Just Accepted” manuscripts.

Electrotunable Nanoplasmonics for Amplified Surface Enhanced Raman Spectroscopy

Ye Ma^{1,2}, Debabrata Sikdar^{1,3}, Aleksandra Fedosyuk¹, Leonora Velleman¹, Daniel J. Klemme⁴, Sang-Hyun Oh⁴, Anthony R.J. Kucernak¹, Alexei A. Kornyshev^{1,5*}, Joshua B. Edel^{1*}

¹Department of Chemistry, Imperial College London, Molecular Sciences Research Hub, White City Campus, London W12 0BZ, UK

²School of Materials Science and Engineering, Ocean University of China, Qingdao, 266100, China

³Department of Electronics and Electrical Engineering, Indian Institute of Technology Guwahati, Guwahati-781039, India

⁴Department of Electrical and Computer Engineering, University of Minnesota, Minneapolis, Minnesota 55455, USA

⁵Thomas Young Centre for Theory and Simulation of Materials, Imperial College London, South Kensington Campus, London SW7 2AZ, UK

Correspondence: a.kornyshev@imperial.ac.uk, joshua.edel@imperial.ac.uk

Abstract

Tuning the properties of optical metamaterials in real time is one of the grand challenges of photonics. Being able to do so will enable a class of adaptive photonic materials for use in applications such as surface enhanced Raman spectroscopy and reflectors/absorbers. One strategy to achieving this goal is based on the electrovariable self-assembly and disassembly of two-dimensional nanoparticle arrays at a metal liquid interface. As expected, the structure results in plasmonic coupling between NPs in the array but perhaps as importantly between the array and the metal surface. In such a system the density of the nanoparticle array can be controlled by the variation of electrode potential. Due to the additive effect, we show that less than 1 V variation of electrode potential can give rise to a dramatic simultaneous change in optical reflectivity from ~93 % to ~1 % and the amplification of the SERS signal by up to 5 orders of magnitude. The process allows for reversible tunability. These concepts are demonstrated in this manuscript, using a platform based on the voltage-controlled assembly of 40 nm Au-nanoparticle arrays at a TiN/Ag electrode in contact with an aqueous electrolyte. We show that all the physics underpinning the behaviour of this platform works precisely as suggested by the proposed theory, setting the electrochemical nanoplasmonics as a promising direction in photonics research.

Keywords: electrotunable, metasurface, plasmonics, surface enhanced Raman spectroscopy, nanoparticles, self-assembly

1
2
3
4 The plasmonic coupling of metallic nanostructures under the excitation of incident light has not only
5 drawn substantial interest,¹⁻³ but also looks promising for applications in optical sensing,⁴⁻⁶ solar energy,⁷
6 biomedical therapy^{8, 9} and especially surface-enhanced Raman spectroscopy (SERS).¹⁰⁻¹⁶ The vibrational
7 Raman fingerprints of target molecules can be enhanced several orders of magnitude, due to the
8 synergistic coupling of localized surface plasmon resonances (LSPR) of nanoparticles (NPs)^{17, 18}, surface
9 modified planar substrates¹⁹ or a combination of both.^{3, 20, 21} Previous reports based on deposited NPs²²
10 or lithographic features^{10, 23} on dry substrates have beautifully demonstrated that the surrounding
11 media,²⁴ metal species,¹¹ size,²⁵ shape,²⁶ interparticle distance^{24, 27} and the gap between the substrate and
12 NPs³ are crucial for the resonance strength, frequency and the resultant SERS signals. The latter is caused
13 by the local near-field enhancement ('hot spots') inside or around these nanostructures.

14
15
16
17 Some of those structures may be fixed/nanofabricated,²⁸ others – self assembled.²⁹ One of the
18 challenges is to adjust the structures *in situ* enabling the tuning of the intensity of the hot spots for
19 maximizing SERS signals.³⁰ Among many methods such as mechanically³¹ or thermally³²⁻³⁴ induced
20 deformation of the nanostructures, or in the case of wet systems – changing pH³⁵ or chemical
21 concentrations³⁶ of the solution can reconfigure the NP assemblies. Particularly interesting is voltage-
22 controlled tuning of the structure of adsorbed NP arrays at electrochemical interfaces.^{37, 38} This causes
23 minimal disturbance to the system, when tuning the plasmonic coupling. By applying different static³⁹ or
24 dynamic⁴⁰ potentials on the substrate electrodes, researchers can either control the adsorption of ions⁴⁰,
25 ⁴¹ or, for potentials outside of the electrochemical windows of such systems, the electron exchange³⁹
26 between NP and the electrodes. Both can affect SERS signals. Our group has previously demonstrated
27 voltage controlled self-assembly of arrays of moderate-size (16 nm) NPs at both liquid-liquid (LLI)⁴² and
28 solid-liquid (SLI)⁴³ interfaces.

29
30
31
32 In this work, we successfully self-assembled 40 nm NP two dimensional arrays onto a TiN-coated Ag
33 electrode-substrate within an optical-electrochemical cell. By controlling the electrode potential, both the
34 optical reflectance and SERS spectra can be tuned in real-time. Importantly, we show that the signal can
35 be amplified due to the coupling of NP's in an array and further amplified due to the coupling between
36 NP array and Ag substrate. This is very much different to the literature based around the coupling of static
37 individual NP's to a metallic substrate as the collective coupling of the NP's in the array in our case results
38 in a red-shift in the coupled plasmon resonance and better matches the Raman excitation wavelength
39 which in turn results in greater SERS intensities. Furthermore, by using our effective media theory (EMT),⁴⁴
40 the optical reflectance spectra can be reproduced allowing us to reveal information about the structure
41 and interparticle spacing of the NP array *in situ*. This could in turn be directly correlated to changes in the
42 SERS intensity. Thus, the results that we present below demonstrate fine tuning of interparticle gaps and
43 the significant amplification of SERS signal. Compared with previously demonstrated SERS active
44 substrates based on NP aggregation, our electrovariable SERS system not only allows for real-time
45 tailorable nanostructures that can be repeatedly used, but also facilitates the extra coupling between the
46 metallic substrate and the NP array, further amplifying the SERS signal.

51 Results and discussions

52 To achieve electrotunability, a planar 125 nm thick Ag substrate with a 5 nm TiN coating acts as the
53 working electrode. A ring-shaped Pt counter electrode and an Ag/AgCl wire reference electrode
54 completes the three-electrode electrochemical cell (Figure S1). The electrodes were embedded in a
55
56
57

1
2
3 solution containing an electrolyte composed of 4-Mercaptobenzoic acid (4-MBA) functionalized 40 ± 3 nm
4 NPs (Figure S2), 20 mM phosphate buffer (PB, pH 6.2) and 20 mM LiCl. A custom-built inverted Raman
5 microscope^{45,46} was used to focus a 632.8 nm He-Ne laser to a diffraction limited spot onto the solid-liquid
6 interface and to collect the Raman spectra. A fibreoptic reflectivity probe⁴⁷ was also integrated into the
7 cell to simultaneously acquire reflectance spectra at the SLI. These spectra not only quantitatively
8 demonstrate the dramatic colour changes during the electro-variable process as we show later, but also
9 provide vital structural information about the nanoscale rearrangement of NPs when compared and
10 'decoded' using our EMT.⁴⁴
11
12

13 The potential of zero charge (PZC) of the TiN/Ag substrate is an essential reference point which governs
14 which potentials are needed to bring NPs to and from the SLI.^{42,43} PZCs of semiconductor covered metals
15 can be determined from their flatband potential, E_{fb} . At the flatband potential, there is no band bending
16 due to surface charges, so that this potential is also the potential of zero charge, namely, $E_{fb} = E_{pzc}$.⁴⁸ By
17 measuring the capacitance of the TiN/Ag as a function of applied electrochemical potential, we
18 determined that the capacitance-potential variation (Figure S4) followed a Mott-Schottky law: $C_{sc}^{-2} \propto E -$
19 $E_{pzc} - k_B T/e$, where C_{sc} is the capacitance of the space charge in TiN, E is the applied potential, E_{pzc} is the
20 potential of zero charge, k_B is the Boltzmann constant, and T the absolute temperature. This linear
21 relationship indicates that the space charge capacitance of the TiN layer dominates the overall
22 capacitance. The PZC was calculated to be -0.8 V vs Ag/AgCl from the intercepts of a linear fit to the data,
23 Figure S4. Henceforth, all potentials are referenced to the PZC, $\bar{E} = E - E_{pzc}$. In order to ensure that our
24 results were not affected by side-reactions at the electrodes, the minimum and maximum electrochemical
25 potential limits were set so as to ensure that the maximum current would not exceed $10 \mu\text{A cm}^{-2}$ over the
26 potential range 0.1 – 0.7 V vs PZC, Figure S5.
27
28
29
30

31 When the potential applied to the substrate is low, an electrostatic energy barrier exists at the SLI,
32 preventing NP assembly, Figure 1a left. As NPs do not assemble on the surface, there is no plasmonic
33 coupling between the substrate and NPs, and hence the corresponding reflectance spectra are identical
34 when compared to pristine TiN/Ag, Figure 1b-ii (black and yellow curves). In addition, no MBA signal could
35 be observed in the Raman spectra, Figure 1c-ii (yellow curve). By switching the substrate to higher
36 potential, 0.7 V vs PZC, the attractive electrostatic forces between the positively charged substrate and
37 the negatively charged NPs construct an energy well in the vicinity of the SLI, and results in the self-
38 assembly of NPs into a two-dimensional array on the substrate, Figure 1a right. This structure results in
39 plasmonic coupling: 1) between NPs within the self-assembled array and 2) between the TiN/Ag substrate
40 and the NP array.
41
42
43

44 Characteristic reflectance and SERS spectra arise from the formation of NP arrays at the SLI. First, the
45 plasmonically active NP array on the substrate almost totally quenched the reflectance at ~ 580 nm as
46 shown in Figure 1b-iii (red curve). Compared with previous studies using smaller, 16 nm NPs,⁴³ the
47 reflectance dip here can be redshifted to 580 nm and deepened to -90 %. More importantly, SERS "hot
48 spots" are formed not only among the NP array but also between the substrate and the array, where the
49 Raman signals of 4-MBA are significantly enhanced. As shown in Figure 1c-iii, the red curve, when 0.7 V vs
50 PZC potential is applied the two characteristic Raman peaks⁴⁹ for 4-MBA at 1078 cm^{-1} and 1589 cm^{-1}
51 significantly increase in intensity.
52
53
54
55
56
57
58
59
60

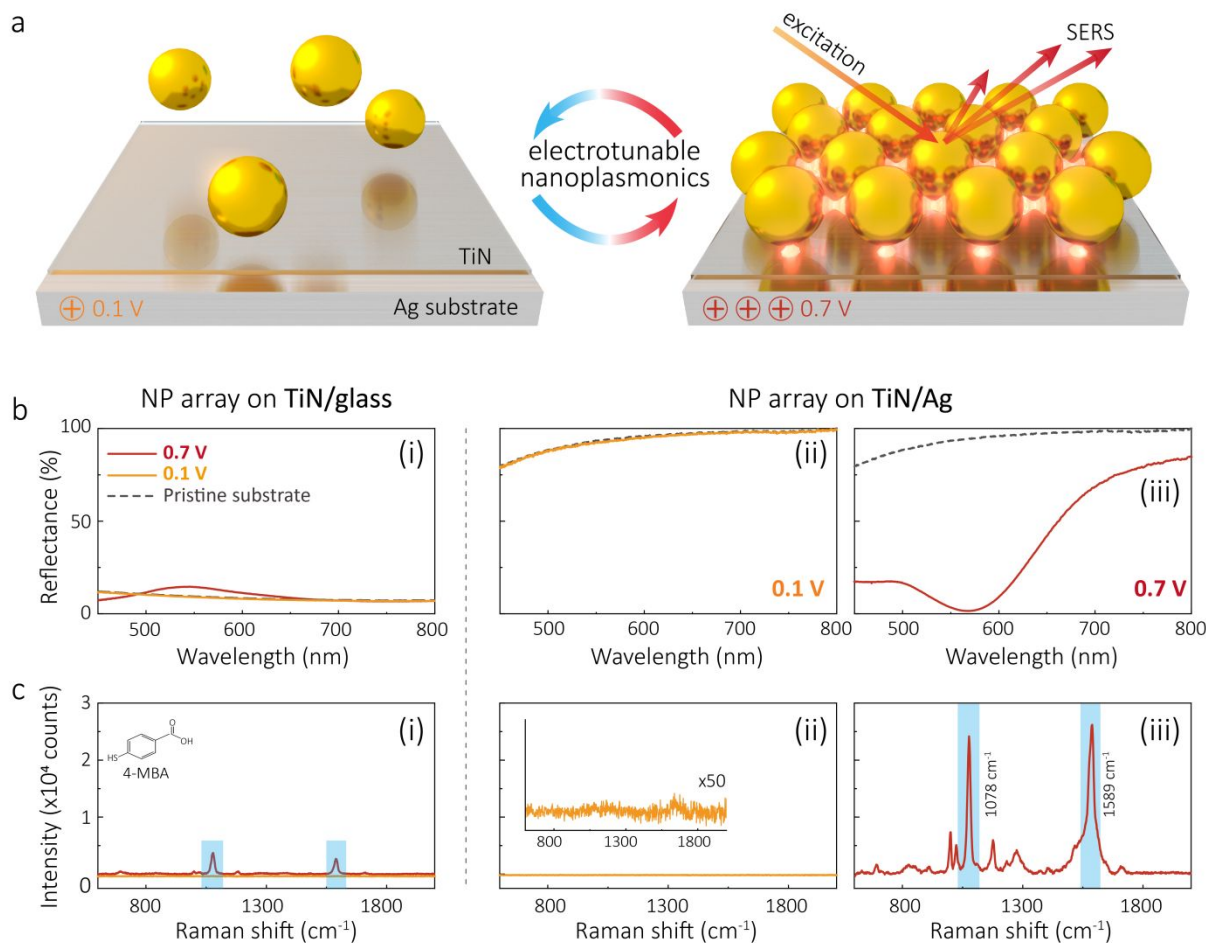


Figure 1 Working principles of electrovariable surface enhanced Raman spectroscopy. (a) Scheme of the experimental setup of the optical-electrochemical cell and the switchable assembly of 40 nm NPs, functionalized by negatively charged 4-MBA ligands, on TiN/Ag substrate under low (left) and high (right) applied voltage. The working electrode of the potentiostat is connected to the substrate, and a Raman microscope is vertically focusing through an optically transparent electrochemical cell. When the applied positive potential of the substrate is low, few NPs are assembled, inducing weak Raman signal (left). Higher positive potential at the interface electrosorbs a monolayer array of NPs which generates Raman hot spots and delivers stronger SERS signals (right), the denser the NP monolayer is. (b-c) The experimental reflectance spectra (b) and SERS spectra (c) of NPs on TiN/glass at 0.1 and 0.7 V vs PZC (i), NPs on TiN/Ag at 0.1 V vs PZC (ii) and NPs on TiN/Ag at 0.7 V vs PZC (iii). The inset of panel c-ii shows the original intensity multiplied by 50 for better visibility. Comparison of these curves highlights the effect of complex plasmonic coupling between the nanoparticles and the metallic substrate. The coupling strengthens with the increase of positive electrode potential that promotes electrosorption of NPs and makes the NP array denser. The significantly enhanced characteristic peaks of 4-MBA at 1078 cm^{-1} and 1589 cm^{-1} indicate the effect of increase and intensification of Raman hot spots in the system.

The plasmonic coupling between metallic NPs has been studied extensively, but the coupling between a metallic substrate and an electro-variable 2D NP array is still intriguing from both experimental and

1
2
3 theoretical viewpoints. In Figures 1b and c, comparisons of optical reflectivity and SERS signals are made
4 between the Au NP array on TiN/glass substrate [Panels (i)] and on TiN/Ag substrate [Panels (ii) and (iii)].
5 It is easy to see a peak in the reflectance spectra of the NPs/TiN/glass at 0.7 V vs PZC (Figure 1b-i), which
6 is very much like that of an array of NPs at the liquid | liquid interface^{42, 47} showing the enhancement of
7 reflectance near the wavelength of the plasmon resonance in the array of gold NPs. On TiN/Ag substrate,
8 the NP array formed under 0.7 V vs PZC, however, quenches the reflectivity of the substrate to such an
9 extent that the reflectance around 580 nm is even lower than for the lone NP array. Both effects are in
10 accordance with our previous studies.⁴²⁻⁴⁴

11
12
13 This phenomenon of quenching of reflection on the NPs/TiN/Ag sample demonstrates the efficient
14 coupling between the array of electrosorbed large, 40-nm NPs and the metallic substrate, which also gives
15 rise to the enhancement of Raman signal. When the array of 4-MBA functionalized NPs is self-assembled
16 on the TiN/glass substrate under 0.7 V vs PZC, the sample gives a distinguishable Raman signal (~3000
17 counts at 1078 cm⁻¹) due to the coupling among the NPs (Figure 1c-i, red curve). By comparison, once
18 those NPs are assembled on the TiN/Ag substrate (under 0.7 V vs PZC), the intensity of the Raman peak
19 increases by ~8.3 fold (Figure 1c-iii), highlighting the synergistic effect between the NP array and the
20 TiN/Ag substrate. Unlike NP aggregates, the interparticle distance could be uniformly controlled bringing
21 about good uniformity and reproducibility of the Raman signal, as shown in Figure S6. Noteworthy, the
22 pH has a significant influence on the stability of the NPs and the density of the NP array assembled at the
23 SLI. As previously reported,^{43, 50} a lower pH reduces the negative charge on the carboxylic acid
24 functionalized NPs, resulting in a greater propensity for NP aggregation, Figure S7 and Figure S8. As shown
25 in Figure S8, a higher pH induces weaker plasmonic coupling: shallower reflectance dip, larger interparticle
26 gap, and lower SERS signal. This is consistent with an increased negative charge and hence increased
27 electrostatic repulsion between the NPs. This in turn results in the formation of less densely packed NP
28 arrays at the SLI. Therefore, to maintain the stability of the NP solution while achieving a good SERS signal,
29 a pH of 6.2 was used for normal operational conditions.

30
31
32 The detailed electro-tunable behaviours of this system were examined through reflectance and SERS at
33 varying potentials. A qualitative view of the effect on NP assembly as a function of potential is shown in
34 the SEM's in Figure 2a. However, it should be noted that the drying process for SEM sample preparation
35 can potentially disturb the arrangement of the wet NPs on the substrates. Nevertheless, an increase in
36 potential results in an increase in NP density. This increased population and its resultant enhanced
37 plasmonic coupling can be visualized by the dramatic changes in the macroscale colours of the wet
38 samples (inset of Figure 2a). Starting from the original silver colour of the pristine substrate, higher
39 potential delivers redder and darker appearance and ultimately a purplish black colour for the 0.7 V vs
40 PZC sample.

41
42
43 Reflectance measurements and theoretical calculations provide more quantitative insight for this
44 electro-variable phenomenon. With the increase of the applied potential, a distinctive reflectance dip gets
45 deeper and red-shifted, as can be seen from excellently matched experimental and theoretical fitted
46 spectra (Figures 2b and c). Within the lower potential region (<0.4 V vs PZC), both the dip depth (Figure
47 S9) and dip wavelength (Figure 2d) change slowly. Theoretical calculation (Figure 2d) indicates that the
48 interparticle distances in these cases are too large to generate effective plasmonic coupling. Further
49 increase in potential induces dramatic optical changes: the dip wavelength red-shifts from 530 nm to 580
50 nm while the dip depth changes from almost zero to -92 %. This can be explained by the strong plasmonic
51 coupling when NPs are getting closer to each other. The reason why they are getting closer was described

by us already.⁴³ At positive electrode potentials, negatively charged NPs get electroadsorbed at the electrode, but as they electrostatically repel each other, they prefer not to come close to each other. With further increase of the positive potential, the driving force for each NPs to be adsorbed at the interface gets stronger, and more NPs adsorb at the electrode, tolerating interparticle repulsion, and hence the NP-array gets denser.⁵¹ Theoretical calculation (Figure 2d) indicates that the interparticle distance, starting from several hundreds of nm at 0.1 V vs PZC, quickly reduces to 20 nm at 0.7 V vs PZC.

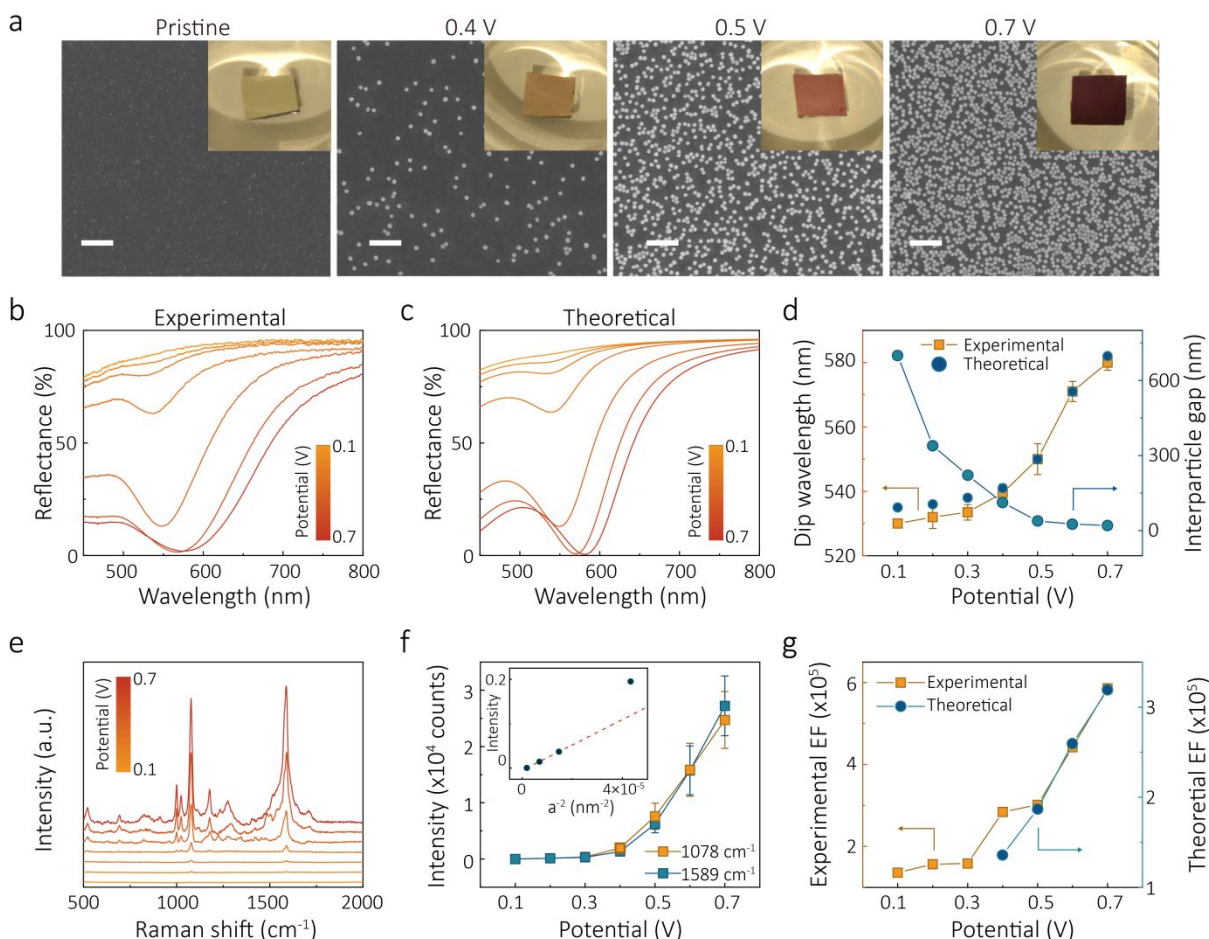


Figure 2 Assembly of nanoparticles by changing the interfacial potentials. (a) SEM of dried samples after NP assembling under indicated potentials; scale bar 200 nm; the white dots represent the adsorbed NPs, shown against the dark background of bare TiN/Ag substrate. Digital camera photos (insets) of wet samples after NP assembly on TiN/Ag under indicated potentials. (b) Experimental reflectance spectra of assembling NPs on TiN/Ag under 0.1 – 0.7 V vs PZC. (c) Theoretically fitted reflectance spectra of assembling NPs on TiN/Ag under 0.1 – 0.7 V vs PZC. (d) The experimental (solid) and theoretically fitted (empty) dip wavelength (orange squares) and the theoretically calculated interparticle gap (blue dots) under 0.1 – 0.7 V vs PZC. (e) Experimental Raman spectra of MBA from the NP array on TiN/Ag under 0.1 – 0.7 V vs PZC. (f) The intensity of characteristic Raman peaks of 4-MBA at 1078 cm^{-1} (orange) and 1589 cm^{-1} (blue) under 0.1 – 0.7 V vs PZC. Inset shows the Raman peak intensity (I) vs the inverse of the square of the interparticle distance (a^{-2}), extracted from fitting the reflectance data to the theory (*c.f.* panel d), in the interval of 0.1 V between 0.1 - 0.4 V vs PZC (g) Experimental (orange squares) and theoretically calculated (blue dots) SERS enhancement factor (EF) under 0.1 – 0.7 V vs PZC. The theoretical EF is not calculated below 0.3 V vs PZC because the gaps are too large to return converging results.

1
2
3 Based on the electromagnetic mechanism of SERS, the variation of the plasmonic coupling due to the
4 change of the interfacial potential also offers a unique and convenient way to enhance the Raman signals.
5 When the potential is low, the two characteristic peaks at 1078 cm^{-1} and 1589 cm^{-1} are almost
6 indistinguishable from the base lines (Figure 2e). The intensity of these peaks climbs gradually (in an
7 almost linear fashion) when the potential is less than 0.4 V vs PZC , but more instructive is the linear
8 dependence on the density of the NP array, which is inversely proportional to the square of interparticle
9 separation, shown in the inset in Figure 2f. Such linear dependence shows that the increase in the SERS
10 intensity here is just due to the increase of the population of NPs and the associated 4-MBA at the
11 interface. As the interparticle gap is large within this potential range (Figure 2d), the coupling between
12 NPs is negligible and so is the increase of the corresponding experimental enhancement factor (Figure 2g),
13 $EF = \frac{I_{\text{SERS}}/N_{\text{SERS}}}{I_{\text{RS}}/N_{\text{RS}}}$ (where I_{SERS} and I_{RS} denote the intensity of SERS and Raman signals, N_{SERS} and N_{RS} are the
14 numbers of molecules generating SERS and Raman signals, respectively). In this potential range, each
15 electroadsorbed NP individually delivers a hot spot between it and the substrate. But the hotter ones emerge
16 only at closer approach of NPs due to the coupling of the localised plasmon excitations between the NPs,
17 presumably amplified by the proximity to the metallic substrate.
18
19
20
21
22

23 As the potential increases beyond 0.4 V vs PZC , the intensities of the peaks rocket to ~ 25000 counts at
24 0.7 V vs PZC ; both the experimental and theoretical (*c.f.* Methods) EFs surge quickly to reach beyond 10^5
25 level at 0.7 V vs PZC . This means that the amplification of the SERS signal benefits majorly not only from
26 the increased number of NPs and 4-MBA molecules, but from the ever-growing plasmonic coupling with
27 gradual red-shift of LSPR towards the excitation laser wavelength.⁵²
28

29 We notice that the experimental EFs are slightly larger than the theoretical ones, where perfectly
30 spherical NPs in a uniform hexagonal lattice is considered for modelling. Considering the existence of
31 edges/spikes on our fabricated NPs and the fact that interparticle gaps may have some dispersion and
32 spatial non-uniformity, a small population of NPs with narrow local interparticle gaps could generate much
33 stronger SERS signals that would contribute to larger experimental values of EF.^{26, 36}
34
35

36 The time evolution of the optical response and SERS signals were also monitored during the potential
37 controlled assembly of NPs on the substrates. Figures 3a and b demonstrate the experimental and
38 theoretically fitted reflectance spectra over 10 h when both the dip wavelength (Figure 3c) and dip depth
39 (Figure S10) first experience a fast evolution stage before reaching the equilibrium plateau at the 580 nm
40 wavelength and -92% intensity. A similar trend in plateauing can be found in the theoretically calculated
41 interparticle gaps. Compared to similar systems with smaller NPs, the time of reaching the equilibrium for
42 our 40 nm NPs is longer, due to their larger diameter and correspondingly smaller diffusion coefficient
43 (usually following the Stokes–Einstein equation).⁵³ Nevertheless, higher NP concentrations and shorter
44 diffusion lengths in miniaturized setups could accelerate this process for practical applications.
45
46
47
48
49
50
51
52
53
54
55
56
57
58
59
60

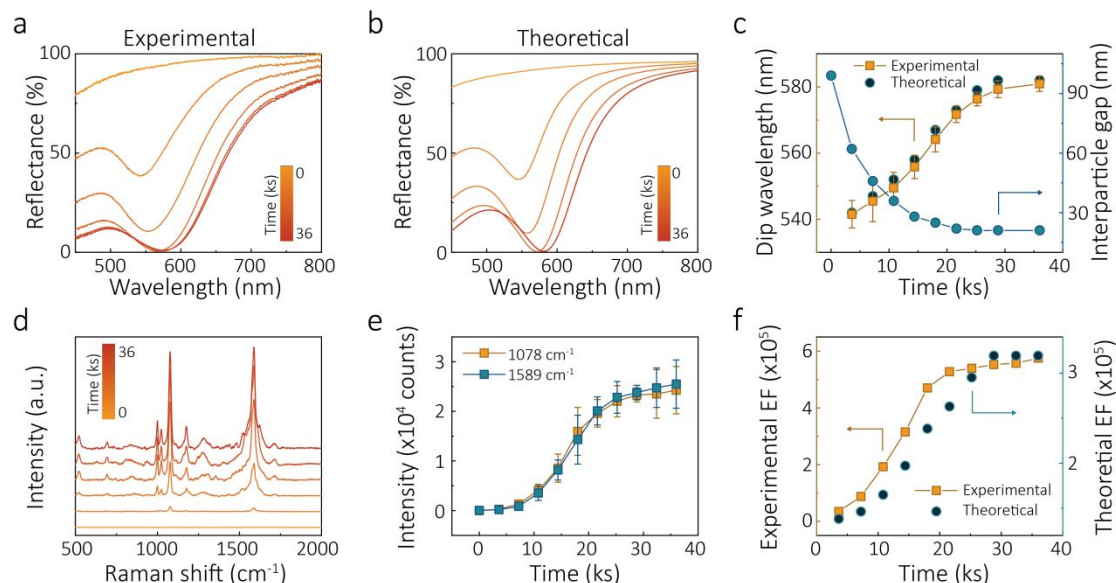


Figure 3 Kinetics of nanoparticle assembly. (a) The time-dependent reflectance spectra of NPs electrosorbed on TiN/Ag in 20 mM PB, 20 mM LiCl NP solution, under 0.7 V vs PZC, starting from pristine TiN/Ag. (b) The theoretically fitted time-dependent reflectance spectra of NPs assembling on TiN/Ag. (c) The time-dependent experimental (solid), theoretically fitted (empty) dip wavelength (orange squares) and the theoretically calculated interparticle gap (blue dots). (d) The time-dependent SERS spectra of 4-MBA attached to NPs assembling on TiN/Ag in 20 mM PB 20 mM LiCl NP solution under 0.7 V vs PZC, starting from pristine TiN/Ag. (e) The corresponding experimental time-dependent intensity of characteristic SERS peaks of 4-MBA at 1078 cm^{-1} (orange) and 1589 cm^{-1} (blue). (f) The time-dependent experimental (orange squares) and theoretically calculated (blue dots) SERS enhancement factors (EF) under 0.7 V vs PZC, starting from pristine TiN/Ag.

It should be emphasized again, that as we have seen first in Figure 1b, Figures 2b and 3a demonstrate the counter-intuitive effect of quenching of reflection from an array of large NPs on metallic substrates at the wavelength of the coupled plasmon resonance, the signatures of which have been predicted earlier theoretically.^{44, 54, 55} The change in SERS signal follows a slightly different pattern after the abrupt application of the positive bias (Figure 3d). Unlike the fast quenching process of the reflectivity in the initial stage, the intensities of the Raman peaks grow relatively slow (Figure 3e). Generally speaking, the plasmonic coupling and the resultant Raman enhancement prevail only when the gaps between NPs are below the NP diameter.⁵⁶ Considering the interparticle gaps in the first 14 ks is still larger than this value (Figure 3c), the Raman hot spots in these gaps are still too weak to generate a noticeable enhanced Raman signals than the individual NPs. However, this hot spot effect becomes more dominant after 14 ks when the gap falls below 40 nm. The calculated experimental and theoretical EFs in Figure 3f support this observation.

The electro-tunability and reversibility of SERS signal is always desirable for reusable sensors, for lasers with different working frequencies or sensing different analytes. Though larger NPs provide stronger SERS amplifications, it is harder to achieve reversibility with larger NPs as compared to smaller ones, due to the reduced diffusion speed of the former.⁵⁷ Here by alternatively applying ± 0.7 V vs PZC to the substrate, we partially achieved turning the system on and off for multiple times. As shown in Figure 4a, under the 'off state' at -0.7 V vs PZC, the plain substrate has a pink tint and the red letter 'IC' (standing for Imperial

College) above the substrate is reflected distinctively. In contrast to that, the substrate becomes almost black and the 'IC' is overwhelmed by the dark background under the 'on state' at 0.7 V vs PZC.

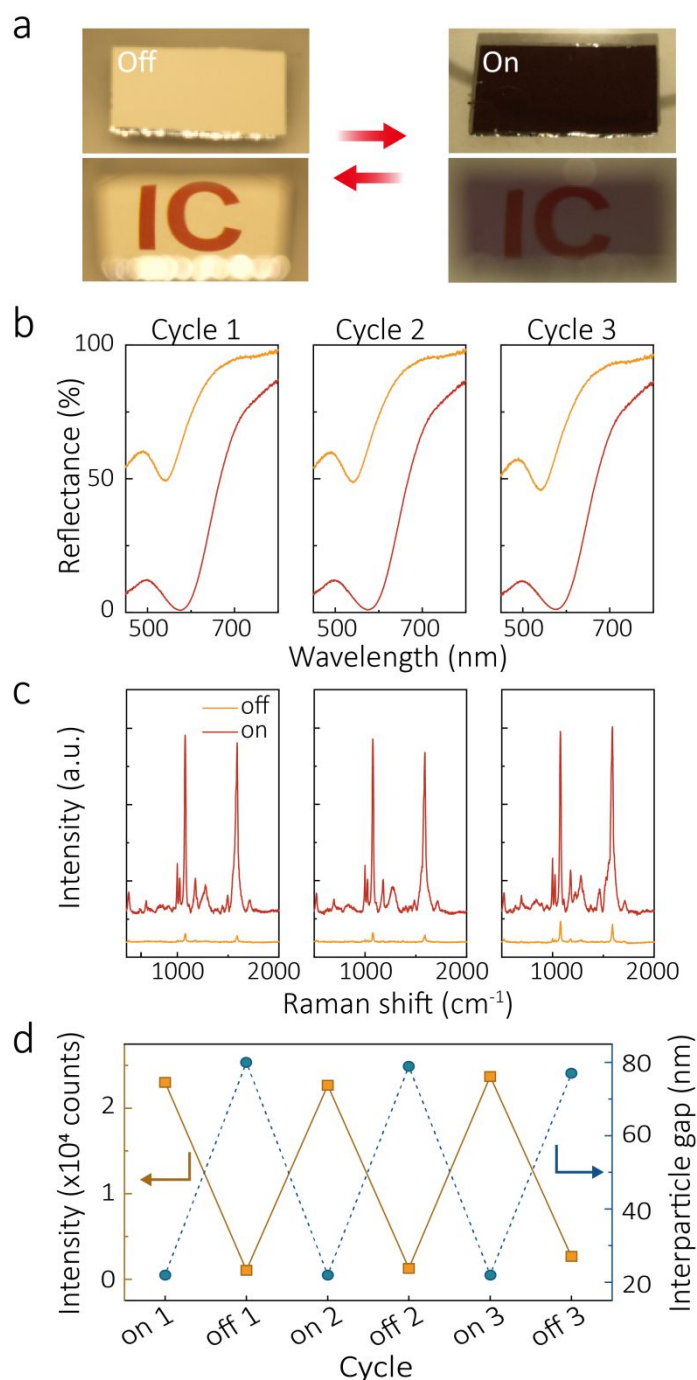


Figure 4 Reversible switching of the nanoparticles at the solid liquid interface. To switch off the system, a low potential (-0.7 V vs PZC) is applied to the substrate and maintained for 5 min. **(a)** The digital camera photos of the 'off' and 'on' states of the system in solution with plain (upper), and "IC" reflected (lower) images. The letters are drawn on A4 paper in red and are illuminated by white light. **(b)** Reflectance spectra of NP array on TiN/Ag substrate during multiple on/off cycles. **(c)** Raman spectra of 4-MBA from

1
2
3 NP array on TiN/Ag substrate during multiple on/off cycles. (d) The Raman intensity (orange) and the
4 calculated interparticle gaps (blue) for multiple on/off cycles.
5

6 The cycling of the reflectance spectra as shown in Figure 4b and Figure S11 demonstrate that the 'on
7 state' is always reversible. However, in the electrode potential range that we have studied under the 'off
8 state', there are always a few NPs stuck at the interface. This results in a small reflection dip and small
9 Raman peaks. Fitting the theory of the optical spectra to the measured reflectance data provides
10 evidence (Figure 4d) that the 'off state' corresponds to an 80 nm interparticle gap. To summarise, at -0.7
11 V the majority of NPs desorb from the solid interface to the bulk; however, some remain behind. Had we
12 been able to apply more negative potentials, we would have expected to have no NPs left at the interface.
13 It cannot be excluded, however, that for more negative potentials, there could be some metastable well,
14 which could kinetically trap NPs at the interface [*c.f.* kinetics of collective desorption of NPs].⁴³
15
16
17

18 Importantly much like conventional SERS substrates, the platform could be used to simultaneously
19 detect and distinguish multiple analytes. This was shown for NPs functionalized with 2-mercapto-5-
20 nitrobenzimidazole (MNBI), malachite green isothiocyanate (MG) and MBA, Figure S12. In addition, we
21 also examined the influence of serum to the Raman signal of the assembled MBA functionalized NPs. As
22 shown in Figure S13, no additional peaks could be observed after the addition of serum, though the
23 intensity of MBA peaks are slightly reduced likely due to scattering of the suspension. Nevertheless, this
24 platform opens the door to the possibility of using such systems for biosensing applications.
25
26

27 Conclusions

28 We investigated the optical response of electro-tunably assembling a two-dimensional array of Au NPs
29 on a TiN/Ag electrode under different electrode potentials. Increasing positive polarization of the
30 electrode stimulates adsorption of negatively charged nanoparticles, decreasing interparticle separations
31 in the array. The narrowing of the interparticle gaps strengthens the plasmonic coupling between NPs.
32 As a consequence, it produces three related effects: 1) The emergence of the dip in reflection spectrum,
33 which gets deeper and its wavelength shifts to the longer wavelength with densification of the NP array.
34 2) The emergence and further intensification of 'hot spots' (for electric field of electromagnetic radiation)
35 between NPs, in addition to the hot spots between individual NPs and the substrate. 3) The red-shifting
36 of the coupled plasmon resonance of the thus assembled NPs towards the wavelength of Raman
37 excitation laser further amplifies SERS signal from analytes attached to NPs.
38
39
40

41 The theory of reflection signal from such systems allows us to quantify the values of interparticle gaps
42 at any applied potential and use this information to estimate the SERS enhancement factor. The SERS data
43 appear to be in full harmony with the reflectivity data. The experimental results show the earlier
44 theoretically predicted counter-intuitive phenomenon — *complete quenching of reflection* from an array
45 of large NPs on metallic substrates at the wavelength of the coupled plasmon resonance.
46
47

48 An outlook of this system is to miniaturize it into microscale chips. This will not only hasten the
49 switching speed, but also provide an opportunity to be coupled with microfluids feeding different kinds
50 of NPs targeting/reporting different analytes, which offers a promising approach of high-throughput
51 optical sensing with electro-tunability and reusability.
52
53
54
55
56
57

Methods

Materials and experimental setup

4-MBA capped 40 nm gold nanoparticles. First, 16 nm NPs were synthesised according to the Frens⁵⁸ method: A solution of 500 ml 0.01 wt% HAuCl₄ was heated to boil with magnetic stirring, followed by the injection of 10 ml of 1 wt% sodium citrate, which was kept for 30 min to allow the reaction to finish. The resultant red NP solution was then cooled to room temperature. Then 40 nm NPs was synthesised according to the Brown method.⁵⁹ Namely, 540 ml water was mixed into 60 ml previously obtained 16 nm NP solution. Followed by the addition of 6 ml 0.2 M NH₂OH·HCl, 5 ml 1 wt% HAuCl₄ was quickly injected with vigorous stirring. After the reaction finished, 612 μl 10 mM solution of 80% 4-mercaptobenzoic acid (MBA), 20% 12-mercaptododecanoic acid (MDDA) was added into the solution which was allowed 12 h for functionalization. Centrifugation of the NPs were performed at 3000 rpm for 1 h and refilled with DI water. We checked the diameter of NPs (Figures S2a) by transmission electron microscope (TEM, JEOL 2100 PLUS), the absorption spectra (Figure S2c) of NPs by a UV-vis spectrometer (Nanodrop 2000, Thermo Scientific), and the presence of NPs on substrates by scanning electron microscope (SEM, LEO Gemini 1525 FEGSEM).

Functionalization with 2-mercapto-5-nitrobenzimidazole (MNBI) and malachite green isothiocyanate (MG). MNBI and MG functionalized NPs were prepared as follows: 612 μl 10 mM solution of 80% MBNI, 20% MDDA or 612 μl 1 mM MG and 10 mM MDDA solution was added into the 40 nm citrate functionalized NP solution respectively and allowed 12 h for functionalization. The dual functionalized MBA-MBNI or MBA-MG NPs were prepared by adding 100 nM MBNI or MG into the above-mentioned MBA NP solutions respectively and allowed to rest for 12 h prior to centrifugation.

TiN/Ag substrates. Similar with previous plasma-enhanced atomic layer deposition (PEALD) method,⁴³ silicon substrates were first stripped of their native oxide layer in a hydrofluoric acid bath. A 2 nm Ti adhesion layer was then evaporated onto the substrate, followed by a 125 nm Ag layer. The sample was then immediately placed in a PEALD system (Veeco Fiji[®] system), where 5 nm of TiN was deposited at a temperature of 270°C. The sample was left to cool in the chamber before exposing it to atmosphere in order to avoid excessive oxidation. Before use, the TiN/Ag substrates were intensively rinsed by acetone, ethanol, and DI water.

Coupled electrochemical-optical setup and measurements. A TiN/Ag substrate acting as the working electrode was inserted into a polytetrafluoroethylene (PTFE) holder which connects the substrate with a platinum wire leading to the potentiostat. Two other holes on the holder accommodated the Ag/AgCl reference electrode and platinum counter electrode, to constitute a three-electrode system. A Gamry ref-600 potentiostat was used to control cell polarisation. A purpose-built Raman microscope is based on an optical inverted microscope (IX71, Olympus), to which a spectrograph (Shamrock SR-303i, Andor) and an electron-multiplying charge-coupled device camera (EMCCD, Newton DU970BV, Andor) were connected. An Olympus 20x, NA 0.45 objective (LCPLFLN-LCD) was mounted on the microscope to focus 0.81 mW power from a 632.8 nm laser beam emitted from a HeNe laser (HRP170, Thorlabs, 21 mW). The reflectance spectra were measured using an Ocean Optics reflection probe with a focal length of 2 mm which was placed above the substrate normal to the TiN/Ag substrate. The white light emitted by a tungsten halogen lamp (Ocean Optics) was transmitted through a multimode fibre in the probe, hit the substrate and was collected by an Andor 163 spectrograph fitted with an iDus charge-coupled device. All the optical references are derived from a Thorlabs silver mirror. During the measurements, NP solution with 20 mM

phosphate buffer (pH 6.2) and 20 mM LiCl electrolyte was poured into the cell. The use of phosphate buffer was used to keep the pH stable during the experiments and the LiCl was used to adjust the electrolyte concentration and to provide Cl⁻ ions for Ag/AgCl reference electrode. NPs were found to be more stable in LiCl than in standard NaCl solution (Figure S3). The Gamry potentiostat applied potential to the substrate while the synchronised Andor spectrometer collected the reflected signals from the substrate simultaneously.

Theoretical Methods

Theoretical calculation of optical reflectance spectra. A five-layer stack model, based on our effective medium theory and multi-layer Fresnel reflection scheme, was deployed to theoretically calculate the optical reflectance spectra. The detail of the theoretical model is provided.⁴⁴ The following parameters, conditions and entities were used for the calculations based on that theoretical model: NP radius $R = 20$ nm; normal incidence angle (as the data were obtained at such angle); $\epsilon_1 = 1.78$, representing an aqueous solution as the NP surrounding medium; $\epsilon_2(\omega)$, denoting a fictitious film emulating the Au NP monolayer, calculated using Eq.(5) in Ref.⁴⁴; $\epsilon_3 = 1.78$ for the spacer layer of thickness $h_s = 1$ nm between the NPs and the TiN/Ag substrate; $\epsilon_4(\omega) = \epsilon_{\text{TiN}}$ representing a thin TiN coating, of thickness $h_f = 5$ nm, on top of a 125-nm-thick Ag film substrate characterised by $\epsilon_5(\omega) = \epsilon_{\text{Ag}}$. Note that the Ag substrate is thick enough not to allow any transmittance through it, and hence, it was safe to be modelled as a semi-infinite layer. The parameters of the Drude–Lorentz model⁴⁴ used to describe optical response of Au (eventually used to obtain $\epsilon_2(\omega)$), TiN, and Ag – are provided in the table below:

Table 1. Parameters of the Drude-Lorentz model for Au, TiN, and Ag:

Material	ϵ_∞	$\omega_{p,D}$ (eV)	γ_D (eV)	s_1	$\omega_{p1,L}$ (eV)	$\gamma_{1,L}$ (eV)	s_2	$\omega_{p2,L}$ (eV)	$\gamma_{2,L}$ (eV)
Au	5.975 2	8.8667	0.0379 9	1.76	3.6	1.3	0.95 2	2.8	0.737
TiN [#]	2.667	10.707	0.195	0.195	2.264	0.722	5.31 2	4.894	3.875
Ag	3.718	9.2093	0.02	0.4242	4.284	0.737	-	-	-

[#]The parameters for TiN coating are slightly different to that of the bulk TiN, as these are fitted to match the measured optical reflectance from a bare 5 nm TiN coating on top of an Ag substrate.

Calculation of theoretical SERS EFs. Numerical simulation of the near-field distribution patterns of the Au NP assembly on TiN/Ag substrate provided theoretical estimates of the SERS EFs, calculated as $\max(|\mathbf{E}/E_0|^4)$, where \mathbf{E}/E_0 is the local electric field enhancement factor at the wavelength of the reflectance dip. The full-wave simulations were conducted using the RF module of the COMSOL Multiphysics[®], a commercially available finite-element-method software. In the simulation model perfectly spherical Au nanospheres were arranged in a hexagonal lattice on top of a TiN/Ag-substrate film of the thicknesses specified in the experiments. A unit cell was designed, which extended in both lateral dimensions using periodic boundary conditions to emulate a NP monolayer assembled on the TiN/Ag substrate with large lateral dimensions. Frequency domain solver was deployed for the simulation studies with extremely small meshing, where the maximum and the minimum mesh element size was chosen to be $\lambda/10$ (where

λ is the wavelength of light in that medium) and 1.5 nm, respectively. Such dense meshing incorporates fine structural details of the system in the numerical simulations and hence, allows to make a good estimation of the SERS EFs.

Acknowledgements

The work was supported by an Engineering and Physical Sciences Research Council grant, 'Electrotuneable Molecular Alarm', EP/L02098X/1. J.B.E. also acknowledges receipt of European Research Council consolidator grant (NanoPD). Y.M. has been supported in part by a China Scholarship Council-Imperial Scholarship (201506320194). L.V. and D.S. acknowledge the support of Marie Skłodowska-Curie fellowships, N-SHEAD and S-OMMs, respectively. D.J.K. and S.-H.O. acknowledge support from Seagate Technology through the Centre for Micromagnetics and Information Technologies (MINT) at the University of Minnesota.

Associated content

Supporting Information Available: The setup of the electrochemical cell, TEM and UV-Vis data about gold NPs, the influence of electrolyte, potential of zero charge, cyclic voltammogram, SERS intensity mapping, the influence of pH, static and dynamic dip depth of the reflectance, reversibility, the calculation of EF, detecting multiple analytes through SERS and the Raman spectra of NP array in serum. This material is available free of charge via the Internet at <http://pubs.acs.org>.

The authors declare no competing financial interest.

References

- (1) Sikdar, D.; Kornyshev, A. A. Theory of Tailorable Optical Response of Two-Dimensional Arrays of Plasmonic Nanoparticles at Dielectric Interfaces. *Sci. Rep.* **2016**, *6*, 33712.
- (2) Solís, D. M.; Taboada, J. M.; Obelleiro, F.; Liz-Marzán, L. M.; García de Abajo, F. J. Optimization of Nanoparticle-Based SERS Substrates through Large-Scale Realistic Simulations. *ACS Photonics* **2017**, *4*, 329-337.
- (3) Nayak, D. R.; Bhat, N.; Venkatapathi, M.; Umapathy, S. Signal Enhancement from Tunable SERS Substrates: Design and Demonstration of Multiple Regimes of Enhancement. *J. Phys. Chem. C* **2018**, *122*, 9134-9140.
- (4) Stewart, M. E.; Anderton, C. R.; Thompson, L. B.; Maria, J.; Gray, S. K.; Rogers, J. A.; Nuzzo, R. G. Nanostructured Plasmonic Sensors. *Chem. Rev.* **2008**, *108*, 494-521.
- (5) Domenici, F.; Fasolato, C.; Mazzi, E.; De Angelis, L.; Brasili, F.; Mura, F.; Postorino, P.; Bordi, F. Engineering Microscale Two-Dimensional Gold Nanoparticle Sluster Arrays for Advanced Raman Sensing: an AFM Study. *Colloids Surf., A* **2016**, *498*, 168-175.
- (6) Fasolato, C.; Giantulli, S.; Silvestri, I.; Mazzarda, F.; Toumia, Y.; Ripanti, F.; Mura, F.; Luongo, F.; Costantini, F.; Bordi, F.; Postorino, P.; Domenici, F. Folate-Based Single Cell Screening Using Surface Enhanced Raman Microimaging. *Nanoscale* **2016**, *8*, 17304-17313.
- (7) Giannini, V.; Fernandez-Dominguez, A. I.; Heck, S. C.; Maier, S. A. Plasmonic Nanoantennas: Fundamentals and Their Use in Controlling the Radiative Properties of Nanoemitters. *Chem. Rev.* **2011**, *111*, 3888-3912.
- (8) Jain, P. K.; Huang, X. H.; El-Sayed, I. H.; El-Sayed, M. A. Noble Metals on the Nanoscale: Optical and Photothermal Properties and Some Applications in Imaging, Sensing, Biology, and Medicine. *Acc. Chem. Res.* **2008**, *41*, 1578-1586.

- 1
2
3 (9) Fasolato, C.; Giantulli, S.; Capocefalo, A.; Toumia, Y.; Notariello, D.; Mazzarda, F.; Silvestri, I.;
4 Postorino, P.; Domenici, F. Antifolate SERS-Active Nanovectors: Quantitative Drug Nanostructuring and
5 Selective Cell Targeting for Effective Theranostics. *Nanoscale* **2019**, *11*, 15224-15233.
- 6 (10) Liu, B.; Yao, X.; Chen, S.; Lin, H.; Yang, Z.; Liu, S.; Ren, B. Large-Area Hybrid Plasmonic Optical Cavity
7 (HPOC) Substrates for Surface-Enhanced Raman Spectroscopy. *Adv. Funct. Mater.* **2018**, *28*, 1802263.
- 8 (11) Wang, X. T.; Ma, G. S.; Li, A. R.; Yu, J.; Yang, Z.; Lin, J.; Li, A.; Han, X. D.; Guo, L. Composition-
9 Adjustable Ag-Au Substitutional Alloy Microcages Enabling Tunable Plasmon Resonance for Ultrasensitive
10 SERS. *Chem. Sci.* **2018**, *9*, 4009-4015.
- 11 (12) Xu, Y.; Konrad, M. P.; Lee, W. W. Y.; Ye, Z.; Bell, S. E. J. A Method for Promoting Assembly of Metallic
12 and Nonmetallic Nanoparticles into Interfacial Monolayer Films. *Nano Lett.* **2016**, *16*, 5255-5260.
- 13 (13) Su, D.; Jiang, S. L.; Yu, M. N.; Zhang, G. Z.; Liu, H.; Li, M. Y. Facile Fabrication of Configuration
14 Controllable Self-Assembled Al Nanostructures as UV SERS Substrates. *Nanoscale* **2018**, *10*, 22737-22744.
- 15 (14) Tian, L.; Su, M.; Yu, F.; Xu, Y.; Li, X.; Li, L.; Liu, H.; Tan, W. Liquid-State Quantitative SERS Analyzer
16 on Self-Ordered Metal Liquid-Like Plasmonic Arrays. *Nat. Commun.* **2018**, *9*, 3642.
- 17 (15) Fasolato, C.; Domenici, F.; Sennato, S.; Mura, F.; Angelis, L. D.; Luongo, F.; Costantini, F.; Bordi, F.;
18 Postorino, P. Dimensional Scale Effects on Surface Enhanced Raman Scattering Efficiency of Self-
19 Assembled Silver Nanoparticle Clusters. *Appl. Phys. Lett.* **2014**, *105*, 073105.
- 20 (16) Domenici, F.; Bizzarri, A. R.; Cannistraro, S. Surface-Enhanced Raman Scattering Detection of Wild-
21 Type and Mutant p53 Proteins at Very Low Concentration in Human Serum. *Anal. Biochem.* **2012**, *421*, 9-
22 15.
- 23 (17) Su, M.; Li, X.; Zhang, S.; Yu, F.; Tian, L.; Jiang, Y.; Liu, H. Self-Healing Plasmonic Metal Liquid as a
24 Quantitative Surface-Enhanced Raman Scattering Analyzer in Two-Liquid-Phase Systems. *Anal. Chem.*
25 **2019**, *91*, 2288-2295.
- 26 (18) Lalander, C. H.; Zheng, Y.; Dhuey, S.; Cabrini, S.; Bach, U. DNA-Directed Self-Assembly of Gold
27 Nanoparticles onto Nanopatterned Surfaces: Controlled Placement of Individual Nanoparticles into
28 Regular Arrays. *ACS Nano* **2010**, *4*, 6153-6161.
- 29 (19) Srituravanich, W.; Fang, N.; Sun, C.; Luo, Q.; Zhang, X. Plasmonic Nanolithography. *Nano Lett.* **2004**,
30 *4*, 1085-1088.
- 31 (20) Chen, S.-Y.; Mock, J. J.; Hill, R. T.; Chilkoti, A.; Smith, D. R.; Lazarides, A. A. Gold Nanoparticles on
32 Polarizable Surfaces as Raman Scattering Antennas. *ACS Nano* **2010**, *4*, 6535-6546.
- 33 (21) Wang, X.; Li, M.; Meng, L.; Lin, K.; Feng, J.; Huang, T.; Yang, Z.; Ren, B. Probing the Location of Hot
34 Spots by Surface-Enhanced Raman Spectroscopy: Toward Uniform Substrates. *ACS Nano* **2014**, *8*, 528-
35 536.
- 36 (22) Ding, L.; Gao, Y.; Di, J. A Sensitive Plasmonic Copper(II) Sensor Based on Gold Nanoparticles Deposited
37 on ITO Glass Substrate. *Biosens. Bioelectron.* **2016**, *83*, 9-14.
- 38 (23) Yan, B.; Thubagere, A.; Premasiri, W. R.; Ziegler, L. D.; Dal Negro, L.; Reinhard, B. M. Engineered
39 SERS Substrates with Multiscale Signal Enhancement: Nanoparticle Cluster Arrays. *ACS Nano* **2009**, *3*,
40 1190-1202.
- 41 (24) Kim, I. H.; Kim, J. H.; Choi, J. Y.; Shin, C. H.; Kim, J. H.; Bae, G. T.; Shin, K. S. Tuning the Interparticle
42 Distances in Self-Assembled Gold Nanoparticle Films with Their Plasmonic Responses. *Chem. Phys. Lett.*
43 **2019**, *715*, 91-99.
- 44 (25) Ashley, M. J.; Bourgeois, M. R.; Murthy, R. R.; Laramy, C. R.; Ross, M. B.; Naik, R. R.; Schatz, G. C.;
45 Mirkin, C. A. Shape and Size Control of Substrate-Grown Gold Nanoparticles for Surface-Enhanced Raman
46 Spectroscopy Detection of Chemical Analytes. *J. Phys. Chem. C* **2018**, *122*, 2307-2314.
- 47 (26) Huang, Z. L.; Meng, G. W.; Hu, X. Y.; Pan, Q. J.; Huo, D. X.; Zhou, H. J.; Ke, Y.; Wu, N. Q. Plasmon-
48 tunable Au@Ag Core-Shell Spiky Nanoparticles for Surface-Enhanced Raman Scattering. *Nano Res.* **2019**,
49 *12*, 449-455.
- 50
51
52
53
54
55
56
57
58
59
60

- 1
2
3 (27) Du, Y. X.; Wei, W.; Zhang, X. W.; Li, Y. B. Tuning Metamaterials Nanostructure of Janus Gold
4 Nanoparticle Film for Surface-Enhanced Raman Scattering. *J. Phys. Chem. C* **2018**, *122*, 7997-8002.
- 5 (28) Kanipe, K. N.; Chidester, P. P. F.; Stucky, G. D.; Moskovits, M. Large Format Surface-Enhanced Raman
6 Spectroscopy Substrate Optimized for Enhancement and Uniformity. *ACS Nano* **2016**, *10*, 7566-7571.
- 7 (29) Hill, R. T.; Mock, J. J.; Urzhumov, Y.; Sebba, D. S.; Oldenburg, S. J.; Chen, S.-Y.; Lazarides, A. A.;
8 Chilkoti, A.; Smith, D. R. Leveraging Nanoscale Plasmonic Modes to Achieve Reproducible Enhancement
9 of Light. *Nano Lett.* **2010**, *10*, 4150-4154.
- 10 (30) Edel, J. B.; Kornyshev, A. A.; Kucernak, A. R.; Urbakh, M. Fundamentals and Applications of Self-
11 Assembled Plasmonic Nanoparticles at Interfaces. *Chem. Soc. Rev.* **2016**, *45*, 1581-1596.
- 12 (31) Laible, F.; Gollmer, D. A.; Dickreuter, S.; Kern, D. P.; Fleischer, M. Continuous Reversible Tuning of
13 the Gap Size and Plasmonic Coupling of Bow Tie Nanoantennas on Flexible Substrates. *Nanoscale* **2018**,
14 *10*, 14915-14922.
- 15 (32) Lu, X. F.; Huang, Y. J.; Liu, B. Q.; Zhang, L.; Song, L. P.; Zhang, J. W.; Zhang, A. F.; Chen, T. Light-
16 Controlled Shrinkage of Large-Area Gold Nanoparticle Monolayer Film for Tunable SERS Activity. *Chem.*
17 *Mat.* **2018**, *30*, 1989-1997.
- 18 (33) Han, F.; Vivekchand, S. R. C.; Soeriyadi, A. H.; Zheng, Y.; Gooding, J. J. Thermoresponsive Plasmonic
19 Core-Satellite Nanostructures with Reversible, Temperature Sensitive Optical Properties. *Nanoscale* **2018**,
20 *10*, 4284-4290.
- 21 (34) Ma, Y.; Sikdar, D.; Fedosyuk, A.; Velleman, L.; Zhao, M.; Tang, L.; Kornyshev, A. A.; Edel, J. B. An
22 Auxetic Thermo-Responsive Nanoplasmonic Optical Switch. *ACS Appl. Mater. Interfaces* **2019**, *11*, 22754-
23 22760.
- 24 (35) Curtis, T.; Taylor, A. K.; Alden, S. E.; Swanson, C.; Lo, J.; Knight, L.; Silva, A.; Gates, B. D.; Emory, S.
25 R.; Rider, D. A. Synthesis and Characterization of Tunable, pH-Responsive Nanoparticle-Microgel
26 Composites for Surface-Enhanced Raman Scattering Detection. *ACS Omega* **2018**, *3*, 10572-10588.
- 27 (36) Velleman, L.; Scarabelli, L.; Sikdar, D.; Kornyshev, A. A.; Liz-Marzan, L. M.; Edel, J. B. Monitoring
28 Plasmon Coupling and SERS Enhancement through *In Situ* Nanoparticle Spacing Modulation. *Faraday*
29 *Discuss.* **2017**, *205*, 67-83.
- 30 (37) Edel, J. B.; Kornyshev, A. A.; Urbakh, M. Self-Assembly of Nanoparticle Arrays for Use as Mirrors,
31 Sensors, and Antennas. *ACS Nano* **2013**, *7*, 9526-9532.
- 32 (38) Lumdee, C.; Toroghi, S.; Kik, P. G. Post-Fabrication Voltage Controlled Resonance Tuning of Nanoscale
33 Plasmonic Antennas. *ACS Nano* **2012**, *6*, 6301-6307.
- 34 (39) Di Martino, G.; Turek, V. A.; Lombardi, A.; Szabó, I.; de Nijs, B.; Kuhn, A.; Rosta, E.; Baumberg, J. J.
35 Tracking Nanoelectrochemistry Using Individual Plasmonic Nanocavities. *Nano Lett.* **2017**, *17*, 4840-4845.
- 36 (40) Byers, C. P.; Hoener, B. S.; Chang, W.-S.; Link, S.; Landes, C. F. Single-Particle Plasmon Voltammetry
37 (spPV) for Detecting Anion Adsorption. *Nano Lett.* **2016**, *16*, 2314-2321.
- 38 (41) Zdaniauskienė, A.; Charkova, T.; Matulaitienė, I.; Eicher-Lorka, O.; Matijoška, A.; Skapas, M.; Selskis,
39 A.; Niaura, G. Electrochemical Shell-Isolated Nanoparticle-Enhanced Raman Spectroscopy: Bonding,
40 Structure, and Ion-Pairing of the Positive Charge Bearing Pyridinium Ring Terminated Monolayer at
41 Smooth Gold Electrode. *J. Phys. Chem. C* **2018**, *122*, 1234-1242.
- 42 (42) Montelongo, Y.; Sikdar, D.; Ma, Y.; McIntosh, A. J. S.; Velleman, L.; Kucernak, Anthony R.; Edel, J.
43 B.; Kornyshev, A. A. Electrotunable Nanoplasmonic Liquid Mirror. *Nat. Mater.* **2017**, *16*, 1127-1135.
- 44 (43) Ma, Y.; Zagar, C.; Klemme, D. J.; Sikdar, D.; Velleman, L.; Montelongo, Y.; Oh, S.-H.; Kucernak, A.
45 R.; Edel, J. B.; Kornyshev, A. A. A Tunable Nanoplasmonic Mirror at an Electrochemical Interface. *ACS*
46 *Photonics* **2018**, *5*, 4604-4616.
- 47 (44) Sikdar, D.; Hasan, S. B.; Urbakh, M.; Edel, J. B.; Kornyshev, A. A. Unravelling the Optical Responses
48 of Nanoplasmonic Mirror-on-Mirror Metamaterials. *Phys. Chem. Chem. Phys.* **2016**, *18*, 20486-20498.
- 49
50
51
52
53
54
55
56
57
58
59
60

- 1
2
3 (45) Cecchini, M. P.; Wiener, A.; Turek, V. A.; Chon, H.; Lee, S.; Ivanov, A. P.; McComb, D. W.; Choo, J.;
4 Albrecht, T.; Maier, S. A.; Edel, J. B. Rapid Ultrasensitive Single Particle Surface-Enhanced Raman
5 Spectroscopy Using Metallic Nanopores. *Nano Lett.* **2013**, *13*, 4602-4609.
- 6 (46) Crick, C. R.; Albella, P.; Kim, H.-J.; Ivanov, A. P.; Kim, K.-B.; Maier, S. A.; Edel, J. B. Low-Noise
7 Plasmonic Nanopore Biosensors for Single Molecule Detection at Elevated Temperatures. *ACS Photonics*
8 **2017**, *4*, 2835-2842.
- 9 (47) Velleman, L.; Sikdar, D.; Turek, V. A.; Kucernak, A. R.; Roser, S. J.; Kornyshev, A. A.; Edel, J. B.
10 Tuneable 2D Self-Assembly of Plasmonic Nanoparticles at Liquid|Liquid Interfaces. *Nanoscale* **2016**, *8*,
11 19229-19241.
- 12 (48) McCafferty, E. Relationship between the Isoelectric Point (pHpzc) and the Potential of Zero Charge
13 (Epzc) for Passive Metals. *Electrochim. Acta* **2010**, *55*, 1630-1637.
- 14 (49) Orendorff, C. J.; Gole, A.; Sau, T. K.; Murphy, C. J. Surface-Enhanced Raman Spectroscopy of Self-
15 Assembled Monolayers: Sandwich Architecture and Nanoparticle Shape Dependence. *Anal. Chem.* **2005**,
16 *77*, 3261-3266.
- 17 (50) Capocefalo, A.; Mammucari, D.; Brasili, F.; Fasolato, C.; Bordi, F.; Postorino, P.; Domenici, F.
18 Exploring the Potentiality of a SERS-Active pH Nano-Biosensor. *Front. Chem.* **2019**, *7*, 413-413.
- 19 (51) Zagar, Z.; Rhys-Griffiths, R.; Podgornik, R.; Kornyshev, A. A. On the Voltage-Controlled Assembly of
20 NP Arrays at Electrochemical Solid/Liquid Interfaces. **2018**, *arXiv:1810.05019*, arXiv.org e-Print archive.
- 21 (52) Willets, K. A.; Duyn, R. P. V. Localized Surface Plasmon Resonance Spectroscopy and Sensing. *Annu.*
22 *Rev. Phys. Chem.* **2007**, *58*, 267-297.
- 23 (53) Kalathi, J. T.; Yamamoto, U.; Schweizer, K. S.; Grest, G. S.; Kumar, S. K. Nanoparticle Diffusion in
24 Polymer Nanocomposites. *Phys. Rev. Lett.* **2014**, *112*, 108301.
- 25 (54) Kornyshev, A. A.; Marinescu, M.; Paget, J.; Urbakh, M. Reflection of Light by Metal Nanoparticles at
26 Electrodes. *Phys. Chem. Chem. Phys.* **2012**, *14*, 1850-1859.
- 27 (55) Truong, V. V.; de Dormale, B. Optical Absorption in Overcoats of Nanoparticle Arrays on a Metallic
28 Substrate. *Plasmonics* **2011**, *6*, 195-200.
- 29 (56) Ru, E. C. L.; Etchegoin, P. G. Single-Molecule Surface-Enhanced Raman Spectroscopy. *Annu. Rev. Phys.*
30 *Chem.* **2012**, *63*, 65-87.
- 31 (57) Booth, S. G.; Dryfe, R. A. W. Assembly of Nanoscale Objects at the Liquid/Liquid Interface. *J. Phys.*
32 *Chem. C* **2015**, *119*, 23295-23309.
- 33 (58) Frens, G. Controlled Nucleation for the Regulation of the Particle Size in Monodisperse Gold
34 Suspensions. *Nature* **1973**, *241*, 20-22.
- 35 (59) Brown, K. R.; Walter, D. G.; Natan, M. J. Seeding of Colloidal Au Nanoparticle Solutions. 2. Improved
36 Control of Particle Size and Shape. *Chem. Mat.* **2000**, *12*, 306-313.
- 37
38
39
40
41
42
43
44
45
46
47
48
49
50
51
52
53
54
55
56
57
58
59
60

TOC graphic

